

Introduction

The property of thermal inertia (TI) represents the resistance of a material to changes in temperature over the diurnal cycle. It is used to estimate surface properties such as particle size, moisture content, and cementation [1]. TI is calculated directly from the thermal conductivity, thermal capacity, and density of the material. Because these variables cannot be measured using remote sensing data, apparent thermal inertia (ATI) is commonly utilized as an approximation that is calculated from albedo and temperature data [2]. However, the estimation of surface properties such as particle sizes within a pixel is limited by the spatial resolution of the data. Within a pixel, the surface may be dominated by a continuous layer of cobbles or rocks, displaying a moderate ATI, or a simple “checkboard” mixing of larger blocks plus fines, also displaying a moderate ATI. This can occur since the detection of coarse particles can be obscured by overlying fines, so it is critical to improve the accurate estimation of the particle size distribution on the surface using ATI data. Understanding the block size distribution within each pixel on a silicic lava flow using thermal inertia and high spatial resolution visible data will improve our ability to determine block sizes and therefore our understanding of flow emplacement for older and active flows and domes [3].

Location

This study focuses on the rhyolite flows in the Mono Domes chain (California) (fig. 1) [4,5]. The North Coulee flow is covered by deposits ranging in grain size from silt to boulder [6]. Even though minor differences in the trace elements exist, the deposits are considered compositionally homogenous [4,7]. These characteristics allow for a detailed investigation of the relationship between TI values and particle size mixtures within a pixel.

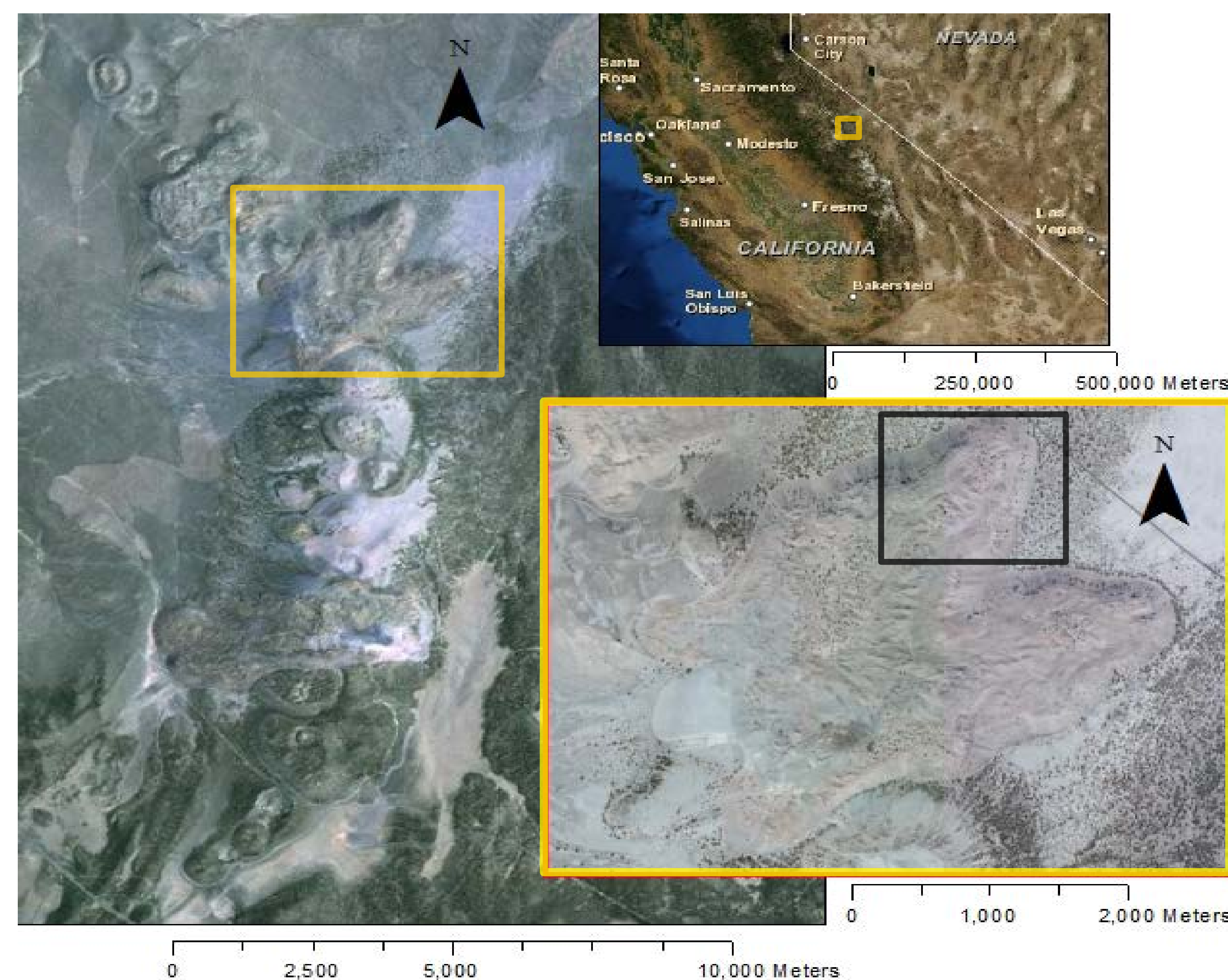


Fig. 1. WorldView2 image of the Mono Craters and Domes site with the yellow rectangle showing the North Coulee flow and black rectangle outlining the location of figure 3 [8]. Context map inset shows the location of the site in eastern-central California.

Datasets

Instrument	Spatial Resolution	Spectral Range	Application
Advanced Spaceborne Thermal Emission and Reflection Radiometer (ASTER)	15m Visible and Near-infrared (VNIR) 90m Thermal Infrared (TIR)	VNIR/TIR	Derive Apparent Thermal Inertia (ATI)
WorldView2 (DigitalGlobe)	50 cm Panchromatic 1.85 m Multispectral	VNIR	Visible analysis of surface roughness
Photogrammetry Digital Terrain Model (DTM)	5cm		Visible and quantitative analysis of surface roughness

Table 1. Datasets used to complete this study with a description of spatial resolution, the spectral range collected by the instrument, and the scientific application of the dataset.

To accurately assess the subpixel distribution of blocks, multispectral data from orbital sensors with spatial resolutions ranging from 50 cm/pixel to 90 m/pixel were analyzed, along with GPS and photogrammetry data acquired in the field (table 1). Field observations and measurements provided ground truth for interpreting TIR data and the properties derived from ATI. To quantify the roughness below the satellite resolution, a DTM was created using over 4000 digital photographs taken of the study site and a ground control points network established using differential GPS. Ground-based multi-view stereophotogrammetry was used to create a 3D point cloud and DTM [9].

Methods

Categories	Particle Size	Visible Image
Coarse	Large blocks	Poorly sorted, Shadowing
Fine	Sand/fine particles	Highly sorted
Mixed	Mix	Intermediate sorting, Minor shadowing
Vegetation	Trees	Individual green objects

Table 2. Four categories with descriptions of the particle size represented by each category and the visible surface features used to identify them.

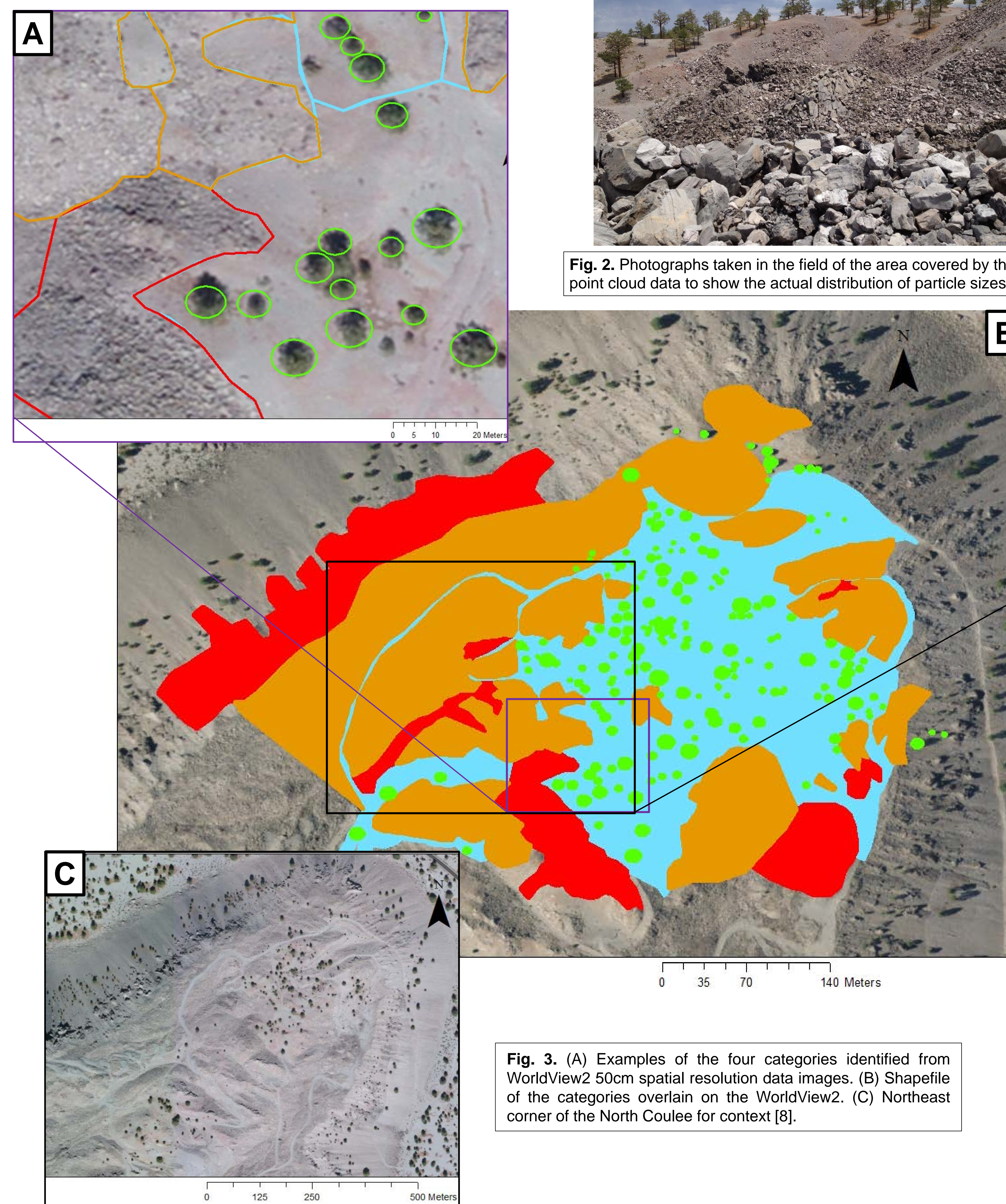


Fig. 2. (A) Examples of the four categories identified from WorldView2 50cm spatial resolution data images. (B) Shapefile of the categories overlain on the WorldView2. (C) Northeast corner of the North Coulee for context [8].

Visible images, with progressively higher spatial resolution, are used to inspect and identify the surface roughness and particle size distribution. Utilizing the point cloud and WorldView2 data, areas are identified that represent the three particle size categories; coarse, fine, and mixed (table 2). The locations of trees are also categorized to assess the influence of vegetation on the ATI product. To identify the category distribution at the 5cm spatial scale, both the DTM and point cloud density data are assessed. The DTM provides the slope change, whereas the point cloud density is ideal for identifying concentrations of rougher surfaces (fig. 3).

An ASTER-derived ATI image is created to assess the thermophysical characteristics of the coulee. The ATI pixels overlying the study are outlined for comparison with the particle size distribution categories. This information is required to further constrain the relationship between subpixel particle size distribution and ATI.

Results

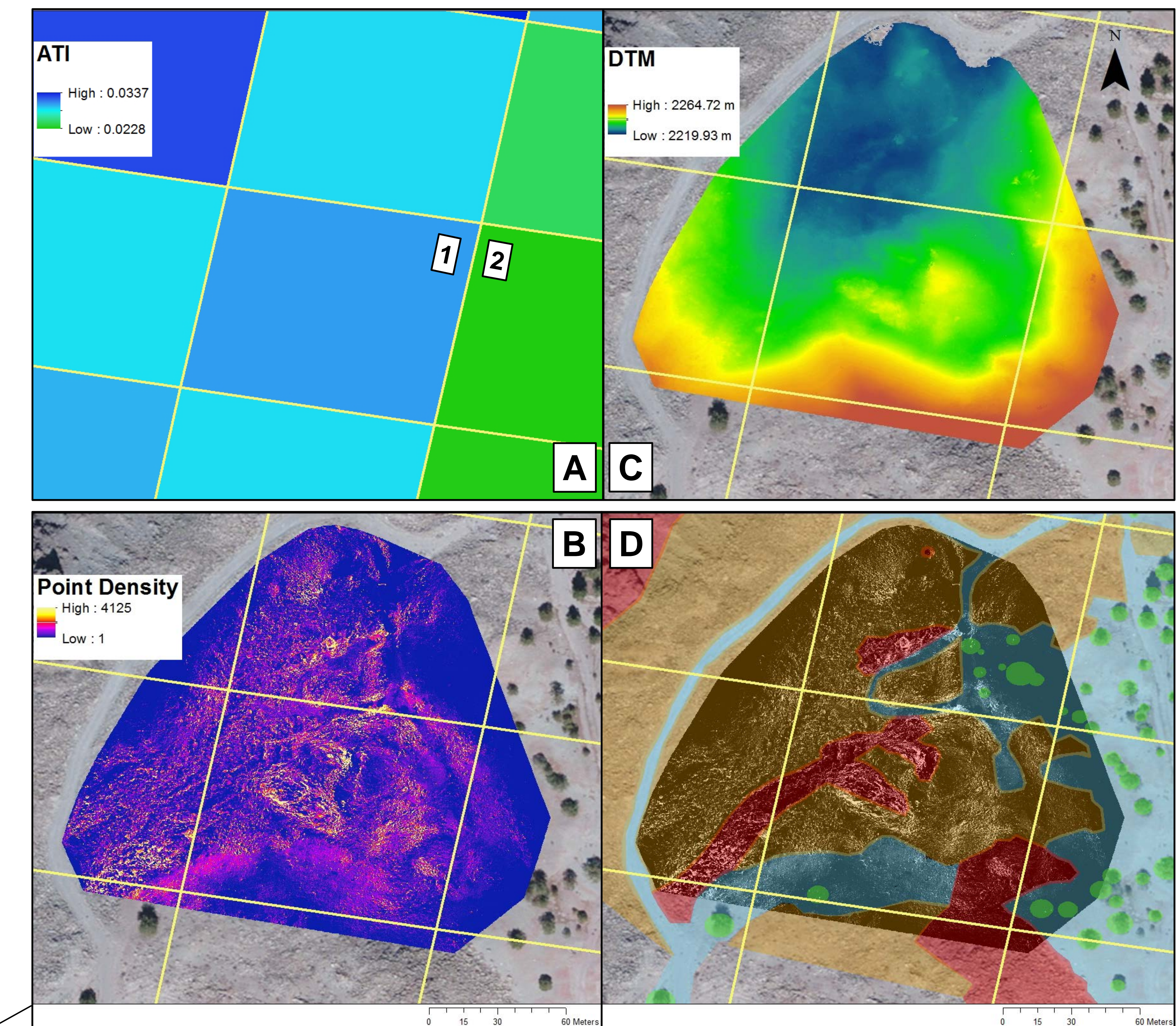


Fig. 3. Study site with the ASTER pixel locations overlain [9]. (A) ATI showing the variation in value over the study site. (B) Point cloud density for visual interpretation of surface particle size distribution (5 cm). (C) DTM, created from the point cloud data. (D) Comparison of point cloud density, category shapefiles defined from WorldView2 data, and ATI overlay on the WorldView2 image to determine the accuracy of particle size identification [8]. Categories: red = coarse, orange = mixed, blue = fine, and green = vegetation.

Application of a multi-instrument, multi-spectral approach combined with thermophysical data provided the information necessary for this study (fig. 4). Analysis of the predicted surface particle size distributions at the different spatial resolutions suggests that WorldView2 data provide very similar results to the highest spatial resolution point cloud data. Comparison of the 5 cm point cloud and the 50 cm WorldView2 category identifications (fig. 4.D) reveals a less than 10% difference that mainly occurs along the edges of the defined categories. This suggests that high resolution orbital data is adequate to accurately assess surface particle size distribution. However, both the DTM and point cloud density (fig. 4.B-C) data are useful to improve the accuracy, particularly at the boundaries.

Furthermore, the high ATI pixel (fig. 4.A, pixel 1) that is entirely covered by the point cloud data (center of fig. 4) suggests the region should contain larger particle sizes. The category distribution shows that over 75% is identified as either mixed or coarse. The neighboring pixel to the right (fig. 4.A, pixel 2) with a low ATI value suggests this area should contain smaller particle sizes. Analysis of the category distribution shows over 80% of the area is identified as fine. Thus, a more detailed quantitative assessment of these category distributions improves the understanding of the relationship between thermal inertia and block size.

Future Work

Current work focuses on comparing the thermal inertia to the particle size distribution seen in the visible data. This will be accomplished by predicting ATI values based on the category percentages within a pixel and comparing the value to the ATI calculated from ASTER data. These results will further constrain the relationship between thermal inertia and block size, so that the lower spatial resolution TIR data alone is sufficient to interpret the thermophysical and surface properties of silicic lava flows. This approach is ideal for understanding surface change with time during active flow emplacement as well as older lava flows on other planets such as Mars.

Acknowledgements

We thank the DigitalGlobe Imagery foundation for the WorldView2 data. This research was funded by the NASA Planetary Geology and Geophysics Program (NNX11AP17G).

References

[1] Hardgrove et al. (2009) *EPSL*, 285, 124-130. [2] Kahle (1987) *Geophy.* 52.7, 858-874. [3] Anderson et al. (1998) *GSA Bulletin*, 110, 1258-1267. [4] Bailey (1989) *JGR*, 81.5, 725-744. [5] Bursik and Sieh (1989) *JGR*, 94.B11, 15587-15609. [6] Sieh and Bursik (1986) *JGR*, 91.B12, 12539-12571. [7] Hildreth (2004) *J. Volc. Geotherm. Res.*, 136.3-4, 169-198. [8] WorldView2 Imagery courtesy of the DigitalGlobe Foundation. (2015) DigitalGlobe Foundation. www.digitalglobe.com. [9] Scheidt et al. (2014) *LPSC*, 45, 1491.